

# Accurate 3D Nanoscale Electromechanical Imaging with a Metrological Atomic Force Microscope

Roger Proksch<sup>1</sup> and Ryan Wagner<sup>2</sup>

<sup>1</sup>*Asylum Research an Oxford Instruments Company, Santa Barbara, CA, 93117 USA*

<sup>2</sup>*School of Mechanical Engineering, Purdue University, West Lafayette, IN, 47907 USA*

---

**ABSTRACT:** We demonstrate an interferometric piezoresponse force microscopy (PFM) method for quantifying the full, three-dimensional response of piezoelectric material without requiring sample rotation. We show that this approach yields quantitative 3D measurement independent of the sample orientation beneath the tip. This approach simplifies existing, angle-resolved PFM techniques, since it only requires four measurements (or three with less redundancy and error checking) to map the full three-dimensional, time independent strain field. It also does not require rotating the sample with respect to the cantilever. It benefits from the greatly reduced noise floor of our laser doppler vibrometer interferometric displacement sensor (IDS) of  $\approx 50\text{fm}/\sqrt{\text{Hz}}$  of our quadrature phase differential interferometer (QPDI) noise floor of  $\approx 5\text{fm}/\sqrt{\text{Hz}}$  and the intrinsic accuracy of interferometric measurements. One important result is that the in-plane piezo sensitivities were systematically smaller than the vertical by a factor  $d_{\text{eff},z}/d_{\text{eff},\text{lat}} \approx 2 - 3$ . A simple analysis of vertical and lateral contact stiffnesses, due to the difference in the Young (vertical) and Shear (lateral) sample moduli predicts a factor of  $d_{\text{theory},z}/d_{\text{theory},\text{lat}} \approx 2.5$ , in good agreement with the measurements. Finally, we fit observed OBD measurements to a linear combination of interferometrically measured in-plane and vertical responses for four different ferroelectric samples. We found that the in-plane response accounted for 20% or more of the OBD response and surprisingly, in two out of the four samples, the in-plane contribution was in fact  $\approx 2x$  larger than the vertical.

---

The accurate characterization of three-dimensional shapes and forces at the nano-scale is critical for advancements across many scientific and technological fields. The atomic force microscope (AFM),<sup>1</sup> because its combination of high resolution, environmental versatility and myriad combined measurement modalities has become a mainstay in nano-science and technology. Typically, AFMs are based around a flexible micromachined cantilever with a sharp tip at the end that localizes the interactions with a sample. Most AFM measurements only measure one strain component of the 3D tip motion vector. This component is typically the vertical deflection component,  $\delta_z$ , of the cantilever away from its equilibrium position. The force can then be estimated from the deflection observable through Hooke's law,  $F_z = k_z \delta_z$ , where  $k_z$  is the spring constant of the cantilever at the tip location and  $\delta_z$  is the displacement of the tip.

The first Atomic Force Microscope (AFM) used a tunneling detector, followed by various interferometric detection methods. In 1986, Martin and Wickramasinghe<sup>2</sup> introduced an AFM with a heterodyne laser interferometer. In 1987, the optical beam deflection (OBD) solution was invented,<sup>3</sup> providing a relatively inexpensive, low-noise detection method that has since become

nearly ubiquitous in the AFM field, with most commercial AFMs based around it. In this method, laser light is focused onto the back of the cantilever, reflected off and detected by a position-sensitive detector. The output signal from the PSD responds when the cantilever undergoes angular displacement, directly proportional to the deflection of the cantilever.

Despite the dominance of the OBD method, there continued to be improvements in interferometric detection. While the noise floor of these interferometers attained impressive levels below 10fm/rtHz<sup>4,5</sup> they suffered from very limited measurement ranges, in the range of a few nm. In 2015, we demonstrated that an interferometric detection system (IDS) could directly probe the motion of an AFM cantilever tip based around a laser vibrometer that had a much higher range of motion.<sup>6</sup> This system has enabled separation of electrostatic interactions and quantification of the inverse piezoresponse in various materials.<sup>7, 8, 9, 10, 11, 12</sup> Very recently, we have released a quadrature phase differential interferometer (QPDI) that has a very low noise floor (~5 fm/rtHz) while maintaining a very large dynamic range (>1um).<sup>13</sup>

Early in the history of PFM, researchers took advantage of lateral detection of OBD based AFMs to image both the vertical and in-plane lateral piezoresponse.<sup>14</sup> By rotating the sample under the probe, a full, three dimensional vector Vector Piezoresponse Force Microscopy<sup>15</sup> (Vector PFM) image can be estimated. Vector PFM measurements based on OBD measurements require precise calibration and data treatment to ensure that the independent x, y and z PFM components. In addition, re-constructing three-dimensional PFM images of polarization is strongly affected by frictional sliding of the tip and longitudinal bending (sometimes inexactly referred to as buckling) of the cantilever.<sup>15, 16</sup> In existing approaches, this process requires careful rotation and relocation of the sample to the same measurement area,<sup>17</sup> which can be difficult and time-consuming. Additionally, thermal drift and repositioning inaccuracies can cause slight differences in the tip position, complicating the alignment of corresponding data points.<sup>18, 19, 20, 17, 21</sup> Finally, those existing works typically struggle to yield quantitative estimation of the in-plane piezoresponse amplitudes, image usually appear with “arbitrary units”, underscoring the challenges of calibrating the OBD sensitivities.

In this work, we demonstrate how interferometric AFM can be extended to quantitatively measure the full, three dimensional response of AFM probes interacting with a sample by mapped the full 3D Piezoresponse Force Microscopy (PFM) response on a variety on ferroelectric samples. PFM measures the local electromechanical response by applying a modulated potential to the cantilever tip and detecting the mechanical response at the same frequency, primarily due to the converse piezoelectric effect.

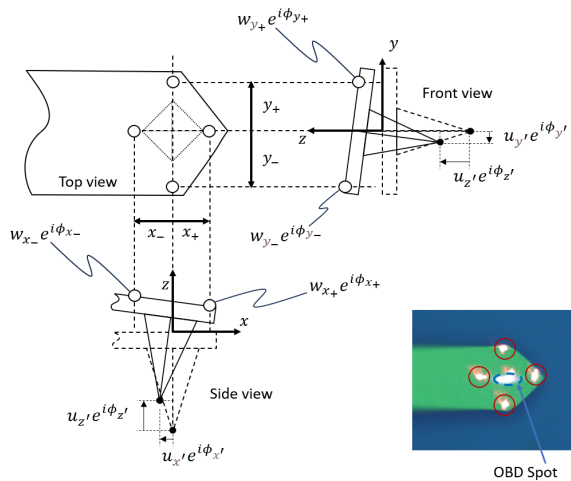


Figure 1 a) shows the end of a cantilever with a coordinate system  $(x, y, z)$  positioned above a sample  $(x', y', z')$ . The displacement of the cantilever on its top surface is described by three . The cantilever can also bend around the longitudinal axis (lateral) The inset shows a composite image with the OBD spot in the center and the composite interferometer spots at the four cardinal positions discussed in the supplemental material.

Single frequency motion of the tip in contact with the sample surface is described by a vector

$$\mathbf{u} = (\hat{x}'u_{x'}e^{i\phi_{x'}} + \hat{y}'u_{y'}e^{i\phi_{y'}} + \hat{z}'u_{z'}e^{i\phi_{z'}})e^{i\omega t}. \quad 1$$

Similarly, we can describe motion of the cantilever along the interferometer measurement axis (z) in response to the tip motion, as

$$W(x, y, t) = w(x, y)e^{i(\omega t + \phi(x, y))} \quad 2$$

Although we can make measurements at many points on the back of the cantilever, for this work, we define displacement measurements at four “cardinal points” as  $w_{x_+} \equiv w(x_+, 0)$ ,  $w_{x_-} \equiv w(x_-, 0)$ ,  $w_{y_+} \equiv w(0, y_+)$  and  $w_{y_-} \equiv w(0, y_-)$ . We also make the measurement points equidistant around the tip location,  $|x_+| = |x_-| = |y_+| = |y_-|$ . If we assume the cantilever is a rigid body, in-plane motion of the tip is translated into tilting of the cantilever body. Then, Equations (1) and (2) can be solved for the amplitudes and phases of the different components (full derivation in the supplemental material) given by

$$u_{x'}e^{i\phi_{x'}} = \frac{(r_0L - x_+)w_{x_+}e^{i(\phi_{x_+} - \phi_{inst})} - (r_0L + x_-)w_{x_-}e^{i(\phi_{x_-} - \phi_{inst})}}{2r_0LG}, \quad 3$$

$$u_{y'}e^{i\phi_{y'}} = \frac{w_{y_+}e^{i(\phi_{y_+} - \phi_{inst})} - w_{y_-}e^{i(\phi_{y_-} - \phi_{inst})}}{2G}, \quad 4$$

$$u_{z'}e^{i\phi_{z'}} = \frac{w_{x_+}e^{i(\phi_{x_+} - \phi_{inst})} + w_{x_-}e^{i(\phi_{x_-} - \phi_{inst})}}{2}, \text{ and} \quad 5$$

$$u_{z'}e^{i\phi_{z'}} = \frac{w_{y_+}e^{i(\phi_{y_+} - \phi_{inst})} + w_{y_-}e^{i(\phi_{y_-} - \phi_{inst})}}{2}. \quad 6$$

In these expressions,  $L$  is the length of the cantilever (base to tip) and  $r_0 = 2/3$  is the dimensionless ratio that determines the effective lever arm length for the zeroth mode of the cantilever. We have made the measurement location equi-distant from the tip location and introduced a geometric factor  $G = |x_+|/h = |x_-|/h = |y_+|/h = |y_-|/h$ , where  $h$  is the height of the tip. In addition, the interferometer spot positions were chosen such that  $G \approx 1$ . The instrumental, frequency-dependent phase offset  $\phi_{inst}$  is assumed to be constant for all of the components and can be determined a number of ways as discussed in the literature.<sup>22, 23, 24</sup> The remainder of the parameters are experimental observables that vary pixel to pixel. If the sample is rotated 90 degrees, as is shown in Figures 2b), 2d), 3b) and 3d) below, transformed equations are given in the supplemental materials (S15-S17).

Equations 3-6 (or S15-S17) provide a full 3D description of the tip motion at the modulation frequency in terms of experimental observables, Note that the  $z'$  component can be estimated from the weighted average of the  $x_+$ ,  $x_-$  or  $y_+$ ,  $y_-$  pairs for both the un-rotated (5 and 6) and rotated (9 and 10) measurements. These independent estimates gives a redundancy test of the time-stability of the sample response and measurements.

In practical measurements with real cantilevers, there is variation in the tip location and dimensions on the cantilever body. These can be characterized with optical or SEM images of the probes. In many cases, these dimensional uncertainties are dominant but even if they are neglected rarely amount to more than 10% uncertainty in the strain measurements (see supplemental materials). While this is significant from many types of physical measurements, one should keep in mind that many current OBD-based calibrations may have uncertainties that are vastly larger; >100% error is not uncommon. It is also interesting to note that while

the vertical strains (Equations 5, 6, 9 and 10) depend on plan-view uncertainties of both the tip and measurement spot locations, since the in-plane measurements rely on differences of the interferometric measurements  $w_j$  and  $\phi_j$ , where  $j = x+, x-, y+, y-$ , they are largely independent on errors in the plan view location of the tip.

In the experimental measurements shown below, we tested the variability associated with the choice of the relative orientation of the sample with the cantilever. Specifically, we rotated samples by 90 degrees so that, for example, the  $x'$  component of the sample was both measured with the detection spots separated along the longitudinal axis of the cantilever (Equation 3) and, in a separate measurement after it was rotated with the spots separated along the lateral axis of the cantilever (Equation 7).

As is common, we define an effective converse piezoresponse sensitivity as  $d_{eff,j} = |u_j|/V_{ac}$ , where the amplitude is  $|u_j| = \left( \sqrt{\text{Re}(u_j e^{i\phi_j})^2 + \text{Im}(u_j e^{i\phi_j})^2} \right)$  and the phase as  $\phi_j = \tan^{-1}(\text{Im}(u_j e^{i\phi_j})/\text{Re}(u_j e^{i\phi_j}))$ , where  $j = x', y'$  or  $z'$  and  $V_{ac}$  is the bias modulation voltage amplitude. We also chose  $\phi_{inst}$  to rotate the measured phasors to range between  $\pi/2$  for positive strain and  $-\pi/2$  for negative strain, therefore allowing separation of positive and negative polarization orientations in histograms (see for example the phasor representation in S??). The final result of the calculations 3-6 or 7-10 are plotted as images of  $d_{eff,j}$  and  $\phi_j$ .

To both verify this approach and to illustrate its application on ferroelectric samples, we adopted the following experimental workflow:

1. Choose a region of the sample and perform four separate interferometric images with the beam positioned at the cardinal points  $(x_+, 0)$ ,  $(x_-, 0)$ ,  $(0, y_+)$  and  $(0, y_-)$  as shown in Figure 1.
  - a. Make the fast-scanning axis for the imaging along the axis perpendicular to the spot position axis (e.g., scan the sample parallel to the  $y$ -axis of the cantilever when making the  $w_{x-}$  and  $w_{x+}$  measurements etc...)
  - b. Adjust scan speeds if necessary to ensure that trace and retrace response curves match to within acceptable experimental uncertainty.
2. Process the measurements according to Equations 3-6 if  $y' \parallel y$  or S15-S17 if  $x' \parallel y$ .
3. As noted in the literature,<sup>25,24</sup> in single frequency PFM, there is typically a frequency-dependent phase shift associated with the control electronics and signal processing of the modulated electromechanical response. This is equivalent to a rotation of the In the case of single frequency PFM, that means we can estimate a phase shift that orients the collective phasor of a series of measurements to be aligned with the in-phase or quadrature axis. This is illustrated in Figure S1

The output of this workflow is shown in Figures 2 and 3 for PZT and BFO respectively. The imaging steps (1 and 3 above) in workflow were executed automatically with a MacroBuilder™ routine. The sample rotation and recentering was accomplished using optical fiducials followed by fine tuning of the scanning locations using the  $x'$  and  $y'$ -offsets in the AFM.

One of our initial questions was whether or not there was a systematic difference in measurements made along the long axis (longitudinal) of the cantilever and measurements made in the transverse (lateral) axis of the cantilever. To test for this rotational variance we rotated the samples of Figures 2 and 3 by 90° around the center of the image area. We performed steps 1-3 that the same reference frame was rotated with respect to the cantilever reference frame. This means that measurements made at cardinal points  $(x_+, 0)$ ,  $(x_-, 0)$  are sensitive to the sample  $y' -$  and  $z' -$  components of the sample strain, while  $(0, y_+)$ ,  $(0, y_-)$  are sensitive to the sample  $x' -$  and  $z' -$  components of the sample strain. In addition to physics differences due to different in-plane stiffnesses of the cantilever tip, comparisons of the original and rotated vector components tests our “rigid body model” of the end of the cantilever.

Figure 2 is a series of sequential images of polished PZT (details in the supplemental material) at two different rotational orientations with respect to the cantilever axes – 0 and 90 degrees. The component images were calculated using Equations (3)-(6). The full data sets are available in the supplemental material Figure S1-S4.

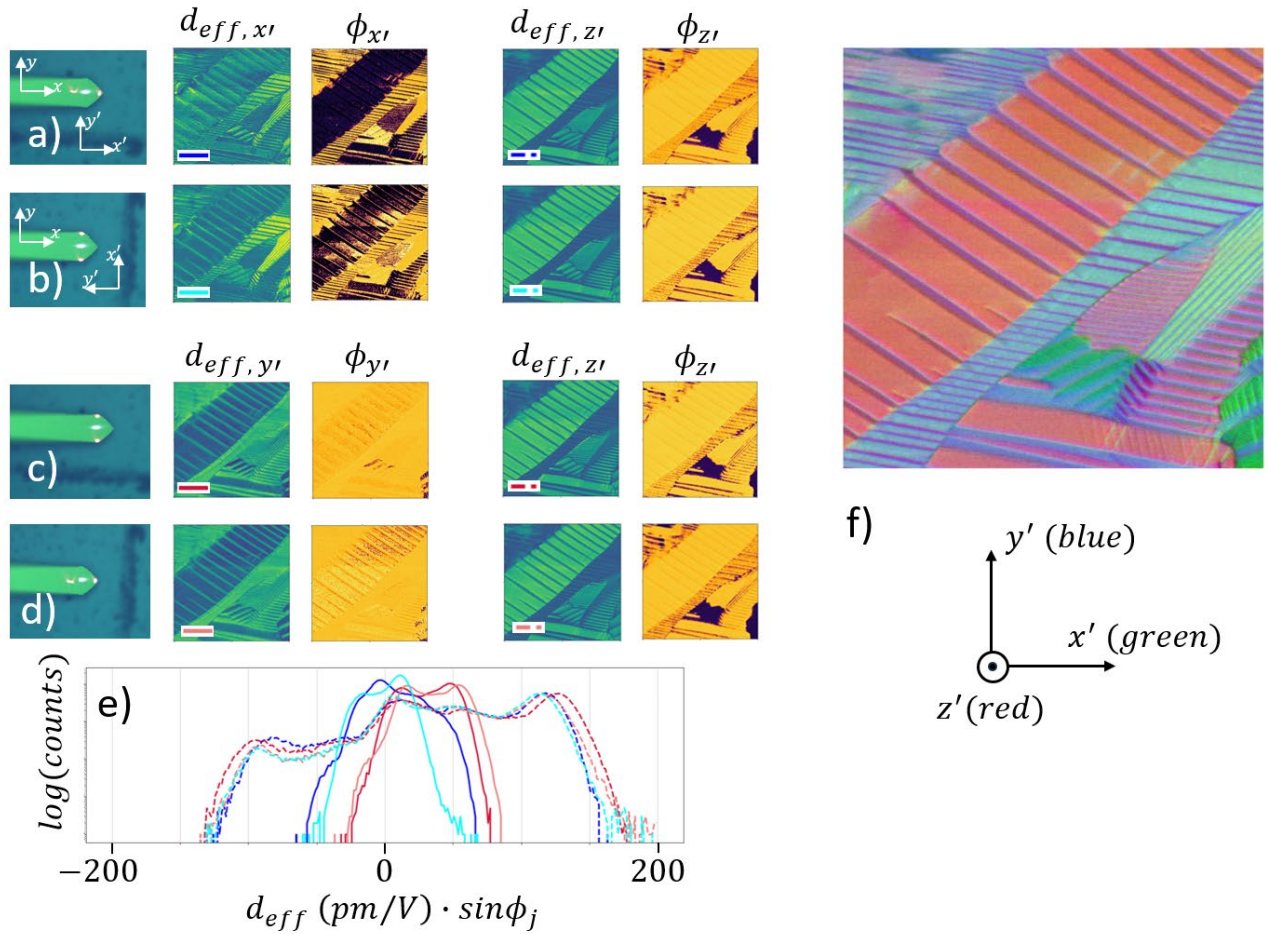


Figure 2. Sequential vector component images of a PZT sample at two different sample orientations. The optical images in a) through d) show the interferometer measurement locations on the top of the cantilever along with the orientation of the sample below it. The measurements were made following the workflow described above. Specifically, a pair of measurements was made for each case a) through d), allowing the estimation of a pair of vector components, one in-plane that depended on the relative alignment of the measurement spots and the sample orientation, and one vertical  $d_{eff, z'}$  and  $\phi_{eff, z'}$ . a) and b) show different measurements of  $x'$  and  $z'$ , while c) and d) show different measurements of  $y'$  and  $z'$ . shows piezoresponse pairs of the converse piezo sensitivity for the in-plan ( $d_{eff, x'}$  and  $\phi_{eff, x'}$ ) and vertical ( $d_{eff, z'}$  and  $\phi_{eff, z'}$ ) measured with spots positioned at  $(x, 0)$  and  $(0, y)$  with the sample at  $0^\circ$  b) the same piezoresponse pairs, measured with the sample at  $90^\circ$  and the measurement spots at  $(0, y)$  and  $(0, y)$ . Similarly, c) and d) show different estimates of the  $y'$  components made by alternating the spot positions and sample rotations. For reference, there is a scratch visible below the cantilever in a) and c) and the right of the cantilever in b) and d) showing the rotation. The color-coded histogram associated with the various effective sensitivity quadrature ( $d_{eff, i} \cdot \sin\phi_i$ ) components are plotted in e).

Comparison of the components; two each of  $x'$  and  $y'$  and four of  $z'$  of the PZT sample in Figure 2 shows a striking similarity between measurements made at different sample orientations. The least similar are the first in-plane components ( $d_{eff, x'}$  and  $\phi_{x'}$ ) in 2a) and 2b). These results support using the simple cantilever model described by Equations 3-6. Conveniently, it also implies that full 3D vector measurements can be made with reasonable confidence *without* rotating the sample. This is a substantial improvement over the current standard approach in AR-PFM.

The histogram plots in 2e) show ranges for the corresponding colorscales in the images. Notably, in Figure 2e), the in-plane components  $x'$  and  $y'$  have a smaller range than do the vertical. Figure 2f) shows a scaled RGB image where each pixel is colored by the sum of the normalized magnitude of the vectoral amplitude.

Returning to the histogram values, the span of the vertical response measurements has a range of  $\approx 300\text{pm}/V$ , while the in-plane is  $\approx 120\text{pm}/V$ . Since the PZT is a sintered polycrystalline material, we expected that there would be a uniform distribution of polarization orientations. The range of the vertical quadrature sensitivity histograms ( $d_{eff, z'} \cdot \sin\phi_{z'}$ , dashed lines in Figure 2e)) are  $\sim 300\text{pm}/V$ , while the range of the in-plane (in-plane,  $d_{eff, x'} \cdot \sin\phi_{x'}$  and  $d_{eff, y'} \cdot \sin\phi_{y'}$ , solid lines in Figure 2e)) is only  $\sim 120\text{pm}/V$ . This  $\sim 2\text{-}3\times$  difference between the vertical and in-plane sensitivity is too large to be explained by geometric uncertainties in Equations (3). Specifically, the largest uncertainty is likely the tip height,  $h \approx 19\mu\text{m} \pm 3\mu\text{m}$  should conservatively lead to only  $\sim 15\%$  uncertainty. This implies that the mismatch between the measured amplitudes may instead have a different origin in the physics of the tip-sample electromechanical contact or another unaccounted compliance such as tip flexing. [ref Joel?]

Figure 3 shows the results of our workflow applied to an epitaxial [100] BFO sample.<sup>26</sup> As with the PZT sample measurements discussed above, we rotated the sample by 90 degrees to characterize the rotational variance (see the sample edge on the bottom of a) and c) and on the right side of images b) and d), performing steps 1-3 in both of the rotational states. In the case of the BFO, inspection of all three spatial components shows excellent correlation, independent of the sample rotation angle. The  $z'$  images in Figure 3 show some variation, however this is mostly an effect of the narrow colorable range. Inspection of the image histograms for  $z'$  (see the color-coded dashed lines in e)) show excellent agreement. The small variations in amplitude of  $z'$  may also be due to small errors in the plan position of the AFM tip (denoted with the diamond shape in Figure 1) or small errors in the positioning of the spots during the measuring step. For example, in the case of the sample being un-rotated, if  $|y_+| \neq |y_-|$ , the  $u_y e^{i\phi_{y'}}$  component will be mixed into the estimated  $u_z e^{i\phi_{z'}}$  component and thereby appear in the  $d_{eff, z'}$  image.



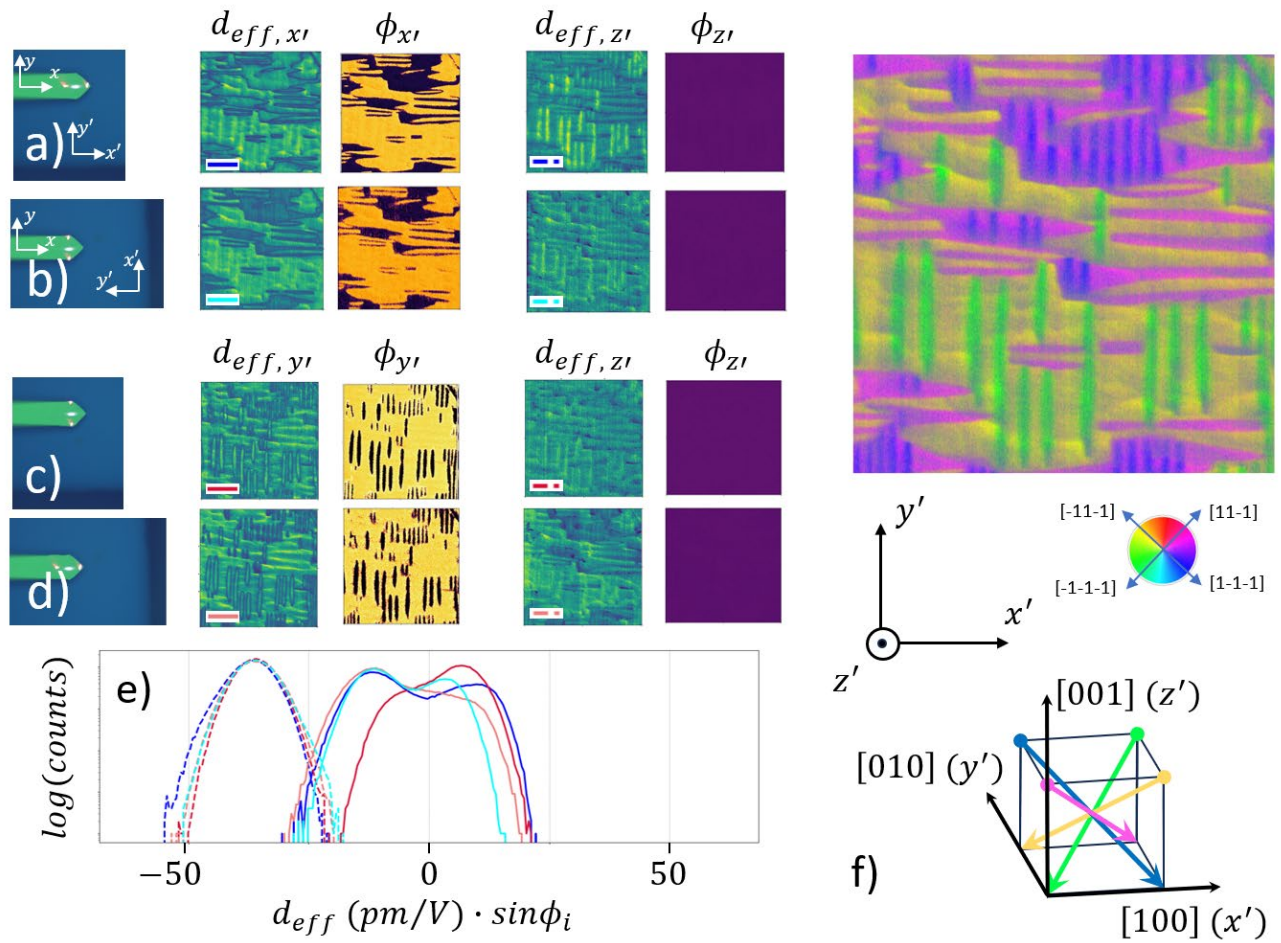


Figure 3. A)-d) show sequential vector component images of BFO made at two different sample orientations using the same workflow as Figure 2. Histograms of the amplitude components are plotted in e). f) illustrates the polarization components along the crystallographic axes of the sample. g) shows the color-coded in-plane vector components derived from the measurement data in a) and c). The original measurement data are shown in the supplemental Figures S5-S8.

In Figure 3, the polarization was found to be in one of four states, along the body diagonal of the unit cell. In all cases, the z-component was oriented into the plane, while there were four in-plane components as shown in Figure 3f). This is in contrast to earlier OBD-based AR-PFM work, where researchers found multiple polarization variants in an unswitched sample.<sup>27, 19</sup>

Note that from the histogram of values in Figure 3e), the span of the out of plane sensitivities has a range of  $\approx 100\text{pm}/V$ , while the in-plane is  $\approx 50\text{pm}/V$ , a similar ratio as the PZT in Figure 2. Finally, Figure 3f) shows a scaled RGB image where each pixel is colored by the sum of the normalized magnitude of the in-plane amplitudes.

One of the goals for this work was to test the self-consistency of vector measurements as the sample was rotated. All three samples show excellent agreement between the vertical component measured at different in-plane orientation angles (Equations 5, 6, 9 and 10). The two samples that were rotated by 90 degrees show excellent agreement between the rotated in-plane components as well, even though in one case the x' component was measured along the x-component of the cantilever and the next along the y-axis of the cantilever. These results validate our cantilever model with a linear beam near the end (see Figure 1).

Quantitative electromechanical response measurements, a long-standing goal for the PFM community, require consideration of the electro-elastic fields generated inside a material due to the contact of a sharp, conductive tip on a piezoelectric sample. Two decades ago, Kalinin et al.<sup>28, 29</sup> discussed the so-called strong indentation case, where the coupled electro-elastic problem for piezoelectric indentation

is solved to obtain the electric field and strain distribution in the ferroelectric material. Specifically, Kalinin et al. predicted a  $d_{eff,z'} \approx 12 \text{ pm/V}$  for the hard indentation limit sensitivity of lithium niobate. While these analytical solutions have contributed to our understanding of PFM contact mechanics and imaging mechanisms, experimental verification of the theoretical predictions have remained elusive until recently, where, through a series of careful interferometric measurements, we were able to experimentally show that in the limit of high indentation forces,  $d_{eff,z'} \rightarrow 12 \text{ pm/V}$  for stoichiometric lithium niobate.<sup>30</sup> Kalinin et al. remained silent on quantifying the in-plane response. In the measurement presented here, the In-plane strain magnitudes,  $d_{eff,x'}$  and  $d_{eff,y'}$  were  $\approx 2 - 3 \times$  smaller than the vertical response. For isotropic solids, we expect that Young's modulus  $E$  is related to the shear modulus  $G$  through the relationship  $E = G(1 + 2\mu)$ , where  $\mu$  is the Poisson's ratio. Furthermore, for a probe in Hertzian contact with the surface, the normal stiffness  $k_z$  is given by  $k_z = 2aE$ , where  $a$  is the contact radius. Similarly, the lateral stiffness is given by  $k_{lat} = 8aG$ .<sup>31</sup> The ratio of these two stiffnesses is therefore  $k_{lat}/k_z = 4/(1 + 2\mu)$ . Since the Poisson ratio of both PZT and BFO is  $\mu \approx 0.3$ , then  $k_{lat}/k_z \approx 2.5$  for both materials. If we assume the strain is inversely proportional to the stiffness, then  $d_{eff,z}/d_{eff,lat} \approx 2.5$ , in reasonable agreement with our experimental observations. Note that this simple calculation neglects friction, an assumption that is clearly violated in many AFM measurements.

In some recent work, we noted that the *presence* of in-plane forces mixing into OBD measurements could be tested by simply varying the scan angle.<sup>30</sup> In the following, we improve on this by using the above methodology to quantify the relative contributions of longitudinal and vertical strains to observed OBD measurements. Figure 4 shows this for four different samples; periodically poled lithium niobate, polished 5A PZT, [011] and [111] PMN-PT. In Figure 4, the first column shows the OBD measured amplitude ( $u_{OBD}$ ) and phase ( $\phi_{OBD}$ ) with the spot placed near the end of the cantilever. The third and fourth columns show the amplitude ( $u_{z'}$  and  $u_{x'}$ ) and phase ( $\phi_{z'}$  and  $\phi_{x'}$ ) of the vertical and longitudinal components, respectively measured using the earlier described methodology. The OBD response,  $u_{OBD}e^{i\phi_{OBD}}$ , can be described by a linear combination of the vertical ( $u_{z'}e^{i\phi_{z'}}$ ) and longitudinal ( $u_{x'}e^{i\phi_{x'}}$ ) interferometric components, along with a constant at each pixel "background" component ( $u_{bg}e^{i\phi_{bg}}$ , not shown as an image) to account for an electrostatic or cross-talk background using standard methods. The linear, real fitting components,  $C_{x'}$ ,  $C_{z'}$  and  $C_{bg}$  were then used to reconstruct the amplitude and phase images  $u_{fit}e^{i\phi_{fit}} = C_{x'}u_{x'}e^{i\phi_{x'}} + C_{z'}u_{z'}e^{i\phi_{z'}} + C_{bg}u_{bg}e^{i\phi_{bg}}$  in Figure 4. The values for the fitting coefficients,  $C_{z'}$ ,  $C_{x'}$ , and  $C_{bg}$  are given in Table I.



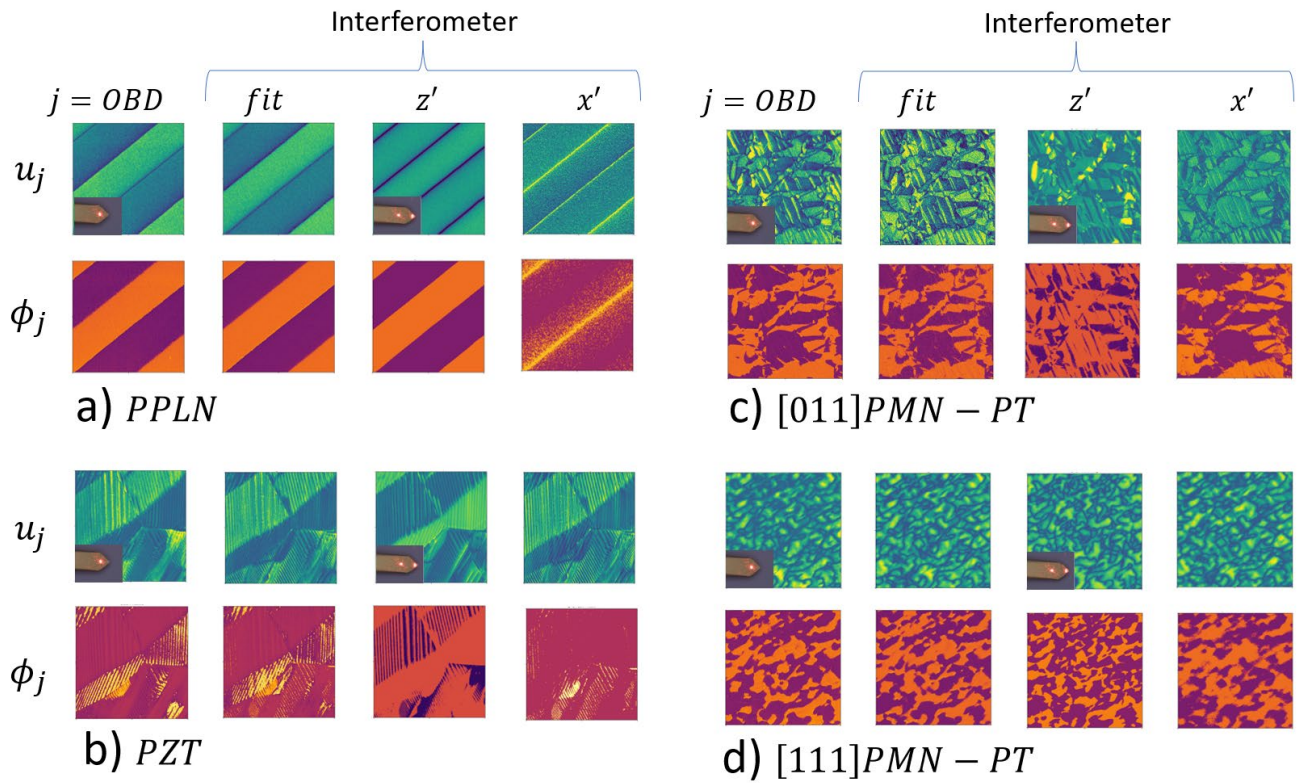


Figure 4. a) shows a comparison of OBD and interferometric vector images for a) PPLN, b) PZT, c) [011] PMN-PT and d) [111] PMN-PT. In all four cases, ( $j = \text{OBD}$ ) show the OBD amplitude (viridis) and phase (inferno) images, ( $j = \text{fit}$ ) shows the fitted vector interferometer response amplitude and phase images that were created from a linear sum of the interferometric vertical ( $j = z'$ ) and longitudinal ( $j = x'$ ) components. More details are given in the text. The fitting coefficients for these samples and additional ones in the supplemental material are shown in Table I.

Sample	$C_x$	$C_z$	$C_{bg}$	$R$
PPLN	19.9%	74.0%	6.1%	0.97
110 PMN-PT	29.3%	65.9%	4.8%	0.81
111 PMN-PT	66.5%	32.0%	1.5%	0.89
PZT 5A	42.6%	23.8%	33.7%	0.65

Table I. Fitting components, expressed as amplitude percentages for four samples shown in Figure 4.

One over-arching result of the measurements shown in Figure 4 is that the OBD PFM measurements (column 1) do not even qualitatively match the vertical response measured with the interferometer (column 3). In all cases, the in-plane, longitudinal contribution accounted for at least  $\sim 20\%$  of the contrast and in two out of the four examples, was the dominant contributor. This is in stark contrast to the usual interpretation that the “normal” OBD signal is primarily due to vertical piezoresponse. This is a non-trivial mixing in the sense that the relative contributions of the in-plane and vertical component is likely to be a function of numerous controlled and uncontrolled experimental parameters including load, scan rates, ranges and angles, humidity.

It is worthwhile pointing out that these results allow the full three-dimensional cantilever motion for static to be more accurately and rapidly measured, there are still uncertainties associated with details of the tip-sample interactions. For example, if the tip is not a

perfect conductor, uncertainties in the contact area remain and must be accommodated in any experimental analysis. Future studies involving varying loads and loading rates for example will help elucidate the competition between conservative and dissipative interactions including in-plane frictional forces. These results and additional measurements using this approach should pave the way for accurate testing of fully three-dimensional theoretical nano-electromechanics.

In conclusion, the sequential interferometric piezoresponse force microscopy (PFM) method introduced here offers a significant advancement in the ability to quantitatively measure the full three-dimensional electromechanical response of piezoelectric materials without the need for sample rotation. By leveraging the reduced noise floor of the interferometric displacement sensor (IDS) and the quadrature phase differential interferometer (QPDI), this approach enables precise and reproducible in-plane and vertical strain measurements. The findings, including a systematic difference in the sensitivities of in-plane and vertical responses, agree well with theoretical models, validating the robustness of this method. Additionally, the ability to map full 3D responses in a time-efficient manner, while minimizing errors associated with sample repositioning, marks a considerable improvement over traditional angle-resolved PFM techniques. This work lays the foundation for more accurate and comprehensive three-dimensional characterization of piezoelectric and ferroelectric materials. Future studies will focus on exploring the complex tip-sample interactions further, particularly with regard to load and frictional effects, to enhance the precision of these measurements even more.

## **ASSOCIATED CONTENT**

### **Supporting Information**

## **AUTHOR INFORMATION**

### **Corresponding Author**

Roger.proksch@oxinst.com

### **Notes**

The authors declare no competing financial interests.

## **ACKNOWLEDGMENT**

RP thanks Gustau Catalan, Sergei Kalinin and Aleks Labuda for useful and informative discussions.

## REFERENCES

---

1. G. Binnig, C. F. Quate and C. Gerber, *Physical review letters* **56** (9), 930 (1986).
2. Y. Martin, C. C. Williams and H. K. Wickramasinghe, *Journal of Applied Physics* **61** (10), 4723-4729 (1987).
3. G. Meyer and N. M. Amer, *Applied Physics Letters* **53** (12), 1045-1047 (1988).
4. D. Rugar, H. J. Mamin, R. Erlandsson, J. E. Stern and B. D. Terris, *Review of Scientific Instruments* **59** (11), 2337-2340 (1988).
5. B. W. Hoogenboom, P. Frederix, D. Fotiadis, H. J. Hug and A. Engel, *Nanotechnology* **19** (38) (2008).
6. A. Labuda and R. Proksch, *Applied Physics Letters* **106** (25), 253103 (2015).
7. Y. T. Liu, L. Collins, R. Proksch, S. Kim, B. R. Watson, B. Doughty, T. R. Calhoun, M. Ahmadi, A. V. Ilevlev, S. Jesse, S. T. Retterer, A. Belianinov, K. Xiao, J. S. Huang, B. G. Sumpter, S. V. Kalinin, B. Hu and O. S. Ovchinnikova, *Nature Materials* **17** (11), 1013-+ (2018).
8. S. S. Cheema, D. Kwon, N. Shanker, R. dos Reis, S. L. Hsu, J. Xiao, H. G. Zhang, R. Wagner, A. Datar, M. R. McCarter, C. R. Serrao, A. K. Yadav, G. Karbasian, C. H. Hsu, A. J. Tan, L. C. Wang, V. Thakare, X. Zhang, A. Mehta, E. Karapetrova, R. V. Chopdekar, P. Shafer, E. Arenholz, C. M. Hu, R. Proksch, R. Ramesh, J. Ciston and S. Salahuddin, *Nature* **580** (7804), 478-+ (2020).
9. L. Collins, Y. T. Liu, O. S. Ovchinnikova and R. Proksch, *Acs Nano* **13** (7), 8055-8066 (2019).
10. Z. M. Zhang, S. L. Hsu, V. A. Stoica, H. Paik, E. Parsonnet, A. Qualls, J. J. Wang, L. Xie, M. Kumari, S. Das, Z. N. Leng, M. McBriarty, R. Proksch, A. Gruverman, D. G. Schlom, L. Q. Chen, S. Salahuddin, L. W. Martin and R. Ramesh, *Advanced Materials* **33** (10) (2021).
11. A. Lipatov, P. Chaudhary, Z. Guan, H. D. Lu, G. Li, O. Crégut, K. D. Dorkenoo, R. Proksch, S. Cherifi-Hertel, D. F. Shao, E. Y. Tsybal, J. Iñiguez, A. Sinitskii and A. Gruverman, *Npj 2d Materials and Applications* **6** (1) (2022).
12. H. D. Lu, H. Aramberri, A. Lipatov, R. Proksch, A. Sinitskii, J. Iñiguez and A. Gruverman, *Acs Materials Letters* **5** (11), 3136-3141 (2023).
13. <https://afm.oxinst.com/products/vero-family-afms/vero-afm>, (2024).
14. M. Abplanalp, L. M. Eng and P. Gunter, *Applied Physics a-Materials Science & Processing* **66**, S231-S234 (1998).
15. S. V. Kalinin, B. J. Rodriguez, S. Jesse, J. Shin, A. P. Baddorf, P. Gupta, H. Jain, D. B. Williams and A. Gruverman, *Microscopy and Microanalysis* **12** (3), 206-220 (2006).
16. R. Nath, S. Hong, J. A. Klug, A. Imre, M. J. Bedzyk, R. S. Katiyar and O. Auciello, *Applied Physics Letters* **96** (16) (2010).
17. K. Chu and C. H. Yang, *Review of Scientific Instruments* **89** (12) (2018).
18. M. Park, S. Hong, J. A. Klug, M. J. Bedzyk, O. Auciello, K. No and A. Petford-Long, *Applied Physics Letters* **97** (11) (2010).
19. M. Park, S. Hong, J. Kim, J. Hong and K. No, *Applied Physics Letters* **99** (14) (2011).
20. K. L. Kim and J. E. Huber, *Review of Scientific Instruments* **86** (1) (2015).
21. B. Kim, F. P. Barrows, Y. Sharma, R. S. Katiyar, C. Phatak, A. K. Petford-Long, S. Jeon and S. Hong, *Scientific Reports* **8** (2018).
22. T. Jungk, A. Hoffmann and E. Soergel, *Journal of Microscopy-Oxford* **227** (1), 72-78 (2007).
23. N. Balke, S. Jesse, P. Yu, B. Carmichael, S. V. Kalinin and A. Tselev, *Nanotechnology* **27** (42) (2016).
24. S. M. Neumayer, S. Saremi, L. W. Martin, L. Collins, A. Tselev, S. Jesse, S. V. Kalinin and N. Balke, *Journal of Applied Physics* **128** (17) (2020).
25. A. Hoffmann, T. Jungk and E. Soergel, *Review of Scientific Instruments* **78** (1) (2007).
26. F. Zavaliche, R. R. Das, D. M. Kim, C. B. Eom, S. Y. Yang, P. Shafer and R. Ramesh, *Applied Physics Letters* **87** (18) (2005).
27. M. Park, S. Hong, J. A. Klug, M. J. Bedzyk, O. Auciello, K. No and A. Petford-Long, *Applied Physics Letters* **97** (11) (2010).
28. S. V. Kalinin, E. Karapetian and M. Kachanov, *Physical Review B* **70** (18) (2004).
29. S. V. Kalinin, E. A. Eliseev and A. N. Morozovska, *Applied Physics Letters* **88** (23) (2006).
30. R. Proksch, R. Wagner and J. Lefever, *Journal of Applied Physics* **135** (3) (2024).
31. A. Makagon, M. Kachanov, S. V. Kalinin and E. Karapetian, *Physical Review B* **76** (6) (2007).